

CRYOSPHERE: SINGLE-PARTICLE HETEROGENEOUS RECONSTRUCTION FROM CRYO EM

000
001
002
003
004
005 **Anonymous authors**
006 Paper under double-blind review
007
008
009
010

ABSTRACT

011 The three-dimensional structure of proteins plays a crucial role in determining
012 their function. Protein structure prediction methods, like AlphaFold, offer rapid
013 access to a protein’s structure. However, large protein complexes cannot be reli-
014 ably predicted, and proteins are dynamic, making it important to resolve their full
015 conformational distribution. Single-particle cryo-electron microscopy (cryo-EM)
016 is a powerful tool for determining the structures of large protein complexes. Im-
017 portantly, the numerous images of a given protein contain underutilized informa-
018 tion about conformational heterogeneity. These images are very noisy projections
019 of the protein, and traditional methods for cryo-EM reconstruction are limited to
020 recovering only one or a few consensus conformations. In this paper, we introduce
021 cryoSPHERE, which is a deep learning method that uses a nominal protein struc-
022 ture (e.g., from AlphaFold) as input, learns how to divide it into segments, and
023 moves these segments as approximately rigid bodies to fit the different conforma-
024 tions present in the cryo-EM dataset. This approach provides enough constraints
025 to enable meaningful reconstructions of single protein structural ensembles. We
026 demonstrate this with two synthetic datasets featuring varying levels of noise, as
027 well as one real dataset. We show that cryoSPHERE is very resilient to the high
028 levels of noise typically encountered in experiments, where we see consistent im-
029 provements over the current state-of-the-art for heterogeneous reconstruction.
030
031

1 INTRODUCTION

032 Single-particle cryo-electron microscopy (cryo-EM) is a powerful technique for determining the
033 three-dimensional structure of biological macromolecules, including proteins. In a cryo-EM exper-
034 iment, millions of copies of the same protein are first frozen in a thin layer of vitreous ice and then
035 imaged using an electron microscope. This yields a micrograph: a noisy image containing 2D pro-
036 jections of individual proteins. The protein projections are then located on this micrograph and cut
037 out so that an experiment typically yields 10^4 to 10^7 images of size $N_{\text{pix}} \times N_{\text{pix}}$ of individual pro-
038 teins, referred to as *particles*. Our goal is to reconstruct the possible structures of the proteins given
039 these images. Frequently, proteins are conformationally heterogeneous and each copy represents
040 a different structure. Conventionally, this information has been discarded, and all of the sampled
041 structures were assumed to be in only one or a few conformations (*homogeneous* reconstruction).
042 Here, we would like to recover all of the structures in a *heterogeneous* reconstruction.

043 Structure reconstruction from cryo-EM presents a number of challenges. First, each image shows a
044 particle in a different, unknown orientation. Second, because of the way the electrons interact with
045 the protein, the spectrum of the images is flipped and reduced. Mathematically, this corresponds to a
046 convolution of each individual image with the Point Spread Function (PSF). Third, the images typi-
047 cally have a very low signal-to-noise ratio (SNR). For these reasons, it is very challenging to perform
048 *de novo* cryo-EM reconstruction. Standard methods, produce electron densities averaged over many,
049 if not all conformations (Scheres, 2012; Punjani et al., 2017), performing discrete heterogeneous re-
050 construction. More recent methods attempt to extract continuous conformational heterogeneity, e.g.,
051 by imposing constraints on the problem through an underlying structure deformed to fit the differ-
052 ent conformations present in the dataset, see e.g. Rosenbaum et al. (2021); Zhong et al. (2021b);
053 Li et al. (2023). AlphaFold (Jumper et al., 2021) and RosettaFold (Baek et al., 2021) can provide
such a structure based on the primary sequence of the protein only. In spite of this strong prior,
it is still difficult to recover meaningful conformations. The amount of noise and the fact that we

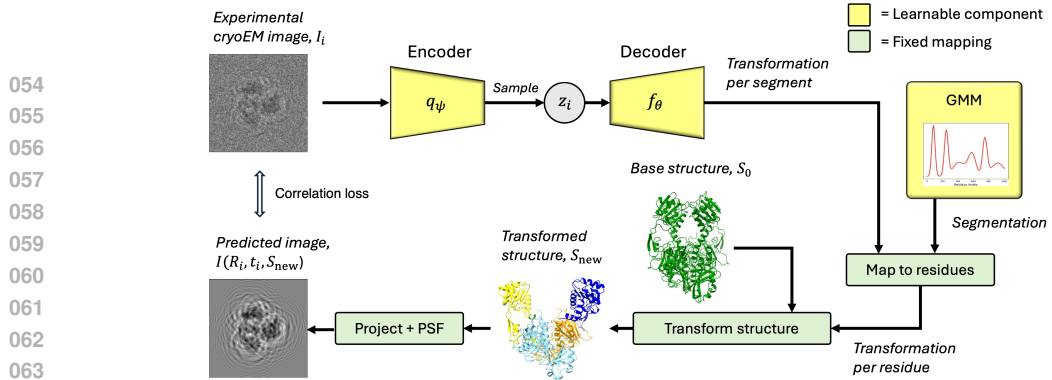


Figure 1: Flow chart of our network. The learnable parts of the model are the encoder, the decoder and the Gaussian mixture. Note that even though the transformations predicted by the decoder are on a per image basis, that is not the case of the Gaussian mixture, which is shared across all particles.

observe only 2D projections creates local minima that are difficult to escape (Zhong et al., 2021b; Rosenbaum et al., 2021), leading to unrealistic conformations.

To remedy this, we root our method in the observation that different conformations can often be explained by large scale movements of domains of the protein (Mardt et al., 2022). Specifically, we develop a variational auto-encoder (VAE) (Kingma & Welling, 2014) that, from a nominal structure and a set of cryo-EM images:

- Learns how to divide the amino-acid chain into segments, given a user defined maximum number of segments; see Figure 2. The nominal structure can for instance be obtained by AlphaFold (Jumper et al., 2021).
- For each image, learns approximately rigid transformations of the identified segments of the nominal structure, which effectively allows us to recover different conformations on an image-by-image (single particle) basis.

These two steps happen concurrently, and the model is end-to-end differentiable. The model is illustrated in Figure 1. The implementation of the model is available on github¹.

Note that what we call a segment is conceptually different from a domain in the structural biology sense. The domains of a protein play a pivotal role in diverse functions, engaging in interactions with other proteins, DNA/RNA, or ligand, while also serving as catalytic sites that contribute significantly to the overall functionality of the protein, see e.g. Schulz & Schirmer (1979); Nelson et al. (2017). By comparison, the segments we learn do not necessarily have a biological function. However, while not strictly necessary for the function of the method, experiments in Section 5 show that our VAE often recovered the actual domains corresponding to different conformations.

2 NOTATIONS AND PROBLEM FORMULATION

In what follows, we consider only the C_α atoms of the protein. A protein made of a number $R_{\text{res}} \in \mathbb{N}^*$ of residues r_i is denoted $S = \{r_i\}_{i=1}^{R_{\text{res}}}$, where the coordinates of residue i are the coordinates of its C_α atom. The electron density map of a structure S , also called a volume, is a function $V_S : \mathbb{R}^3 \rightarrow \mathbb{R}$, where $V_S(x)$ is proportional to the probability density function of an electron of S being present in an infinitesimal region around $x \in \mathbb{R}^3$. That is, the expected number of electrons in $B \subseteq \mathbb{R}^3$ is proportional to $\int_B V_S(x) dx$.

Assume we have a set of 2D images $\{I_i\}_{i=1}^N$ of size $N_{\text{pix}} \times N_{\text{pix}}$, representing 2D projections of different copies of the same protein in different conformations. Traditionally, the goal of cryo-EM heterogeneous reconstruction has been to recover, for each image i , the electron density map V_i corresponding to the underlying conformation present in image i ; see Section 4 for a review of these methods. However, following recent works, e.g., Rosenbaum et al. (2021); Zhong et al. (2021b), we aim at recovering, for each image i , the underlying structure S_i explaining the image. That is, we try to recover the precise position in \mathbb{R}^3 of each residue.

¹anonymous for submission

108 **3 METHOD – CRYOSPHERE**
 109

110 In this section, we present our method for single-particle heterogeneous reconstruction, denoted
 111 cryoSPHERE. The method focuses on structure instead of volume reconstruction. It differs from
 112 the previous (Rosenbaum et al., 2021) and concurrent (Li et al., 2023) works along this line in
 113 the way the movements of the residues are constrained: instead of deforming the base structure
 114 on a residue level and then imposing a loss on the reconstructed structure, our method learns to
 115 decompose the amino-acid chain of the protein into segments and, for each image I_i , to rigidly
 116 move the learnt segments of a base structure S_0 to match the conformation present in that image.
 117 This is motivated by the fact that different conformations of large proteins often can be explained by
 118 large scale movements of its domains (Mardt et al., 2022).

119 The base structure S_0 can be obtained using methods like AlphaFold (Jumper et al., 2021) and
 120 RosettaFold (Baek et al., 2021), based on the amino-acid sequence of the protein. In Section 5, we
 121 further fit the AlphaFold predicted structure into a volume recovered by a custom backprojection
 122 algorithm provided by Zhong et al. (2020).

123 We use a type of VAE architecture, see Figure 1. We map each image to a latent variable by a
 124 stochastic encoder, which is then decoded to a rigid body transformation per segment. Based on
 125 these transformations and the segment decomposition, the underlying structure S_0 is deformed,
 126 posed and turned into a volume that is used to create a projected image. This image is then compared
 127 to the input image. After that, the backward pass updates the parameters of the encoder, decoder
 128 and Gaussian mixture. We now describe the details of our model.

129 **3.1 IMAGE FORMATION MODEL**
 130

131 To compute the 2D projection of the protein structure S , we first estimate its 3D electron density
 132 map V :

$$134 \quad V_S(r) := \sum_{a \in S} A_a \exp\left(-\frac{\|r - a\|^2}{2\sigma^2}\right) \quad (1)$$

136 where A_a is the average number of electrons per atom in residue a , $r \in \mathbb{R}^3$ and $\sigma = 2$ by default.
 137 Hence, the protein’s electron density is approximated as the sum of Gaussian kernels centered on its
 138 C_α atoms. From these density maps, we then compute an image projection $I \in \mathbb{R}^{N_{\text{pix}} \times N_{\text{pix}}}$ as:

$$139 \quad I(R, t, S)(r_x, r_y) = g * \int_{\mathbb{R}} V_{RS+t}(r) dr_z, \quad (2)$$

141 where $(r_x, r_y) \in \mathbb{R}^2$ are the coordinates of a pixel, $r_z \in \mathbb{R}$ is the coordinate along the z axis,
 142 $R \in SO(3)$ is a rotation matrix and $t \in \mathbb{R}^3$ is a translation vector. The abuse of notation $RS + t$
 143 means that every atom of S is rotated according to R and then translated according to t . The image
 144 is finally convolved with the point spread function (PSF) g , which in Fourier space is the contrast
 145 transfer function (CTF), see Vulović et al. (2013). Note that the integral can be computed exactly
 146 for our choice of approximating the density map as a sum of Gaussian kernels, which significantly
 147 reduces the computing time.

148 **3.2 MAXIMUM LIKELIHOOD WITH VARIATIONAL INFERENCE**
 149

151 To learn a distribution of the different conformations, we hypothesize that the conformation seen in
 152 image I_i depends on a latent variable $z_i \in \mathbb{R}^L$, with prior $p(z_i)$. Let $f_\theta(S_0, z)$ be a function which,
 153 for a given base structure S_0 and latent variable z , outputs a new transformed structure S . This
 154 function depends on a set of learnable parameters θ . Then, the conditional likelihood of an image
 155 $I^* \in \mathbb{R}^{N_{\text{pix}} \times N_{\text{pix}}}$ with a pose given by a rotation matrix R and a translation vector t is modeled as
 156 $p_\theta(I^* | R, t, S_0, z) = \mathcal{N}(I^* | I(R, t, f_\theta(S_0, z)), \sigma_{\text{noise}}^2)$, where σ_{noise}^2 is the variance of the observation
 157 noise. The marginal likelihood is thus given by

$$158 \quad p_\theta(I^* | R, t, S_0) = \int p_\theta(I^* | R, t, S_0, z) p(z) dz. \quad (3)$$

160 In practice, the pose (R, t) of a given image is unknown. However, following similar works (Zhong
 161 et al., 2021b; Li et al., 2023), we suppose that we can estimate R and t to sufficient accuracy using
 off-the-shelf methods (Scheres, 2012; Punjani et al., 2017).

162 Directly maximizing the likelihood (3) is infeasible because one needs to marginalize over the la-
 163 tent variable. For this reason, we adopt the VAE framework, conducting variational inference on
 164 $p_\theta(z|I^*) \propto p_\theta(I^*|z)p(z)$, and simultaneously performing maximum likelihood estimation on the
 165 parameters θ .

166 Let $q_\psi(z|I^*)$ denote an approximate posterior distribution over the latent variables. We can then
 167 maximize the evidence lower-bound (ELBO):
 168

$$\mathcal{L}(\theta, \psi) = \mathbb{E}_{q_\psi} [\log p_\theta(I^*|z)] - D_{KL}(q_\psi(z|I^*)||p(z)) \quad (4)$$

170 which lower bounds the log-likelihood $\log p_\theta(I^*)$. Here D_{KL} denotes the Kullback-Leibler (KL)
 171 divergence. In this framework f_θ is called the decoder and $q_\psi(z|I^*)$ the encoder.
 172

173 3.3 SEGMENT DECOMPOSITION

175 To handle the often very low SNR encountered in cryo-EM data, we regularize the transformation of
 176 the structure produced by the decoder by restricting it to transforming whole segments of the protein.
 177 We fix a maximum number of segments $N_{\text{segm}} \in \{1, \dots, R_{\text{res}}\}$ and we represent the decomposition
 178 of the protein by a stochastic matrix $G \in \mathbb{R}^{R_{\text{res}} \times N_{\text{segm}}}$. The rows of G represent "how much of each
 179 residue belongs to each segment", and our objective is to ensure that each residue *primarily* belongs
 180 to one segment, that is:

$$\begin{aligned} \forall i \in \{1, \dots, R_{\text{res}}\}, \exists m^* \in \{1, \dots, N_{\text{segm}}\} \\ \text{s.t. } \sum_{m \neq m^*} G_{im} \ll 1 \end{aligned} \quad (5)$$

185 We also aim for the segments to respect the sequential structure of the amino acid chain, and the
 186 model to be end-to-end differentiable. Without end-to-end differentiability, we could not apply the
 187 reparameterization trick and we would have to resort to Monte Carlo estimation of the gradient of
 188 the segments, which has a higher variance, see e.g. Mohamed et al. (2019).

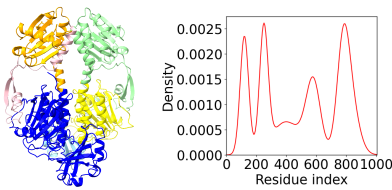
189 To meet these criteria, we fit a Gaussian mixture model (GMM) with N_{segm} components on the real
 190 line supporting the residue indices. Each component m has a mean μ_m , standard deviation σ_m and
 191 a logit weight α_m . The $\{\alpha_m\}$ are passed into a softmax to obtain the weights $\{\pi_m\}$ of the GMM,
 192 ensuring they are positive and summing to one. We further anneal the Gaussian components by a
 193 temperature $\tau > 0$, and define the probability that a residue i belongs to segment m as:

$$G_{im} := \frac{\{\phi(i|\mu_m, \sigma_m^2)\pi_m\}^\tau}{\sum_{k=1}^{N_{\text{segm}}} \{\phi(i|\mu_k, \sigma_k^2)\pi_k\}^\tau} \quad (6)$$

198 where $\phi(x|\mu, \sigma^2)$ is the unidimensional Gaussian probability density function with mean μ and
 199 variance σ^2 and τ is a fixed hyperparameter. If τ is sufficiently large, we can expect condition (5) to
 200 be verified. See Figure 2 for an example of a segment decomposition using a Gaussian mixture.

201 In this "soft" decomposition of the protein, each residue can belong to more than one segment,
 202 allowing for smooth deformations. In addition, the differentiable architecture is amenable to gradient
 203 descent methods, and a well chosen τ can approximate a "hard" decomposition of the protein. We
 204 set $\tau = 20$ in the experiment section. In our experience, this segmentation procedure is very robust
 205 to different initialization and converges in only a few epochs.

206
 207
 208
 209
 210
 211
 212
 213
 214
 215

216 3.4 DECODER ARCHITECTURE
217225 Figure 2: Example of segments recovered
226 with a Gaussian mixture of 6 components.
227228 body transformations, one for each segment $m = 1, \dots, N_{\text{segm}}$. The transformation of segment m
229 is represented by a translation vector \vec{t}_m and a unit quaternion \vec{q}_m (Vicci, 2001), which can further
230 be decomposed into an axis of rotation $\vec{\phi}_m$ and rotation angle δ_m . Second, given the parameters of
231 the GMM, we compute the matrix G . Finally, for each residue i of S_0 , we update the coordinates of
232 all its atoms $\{a_{ik}\}_{k=1}^{A_i}$:

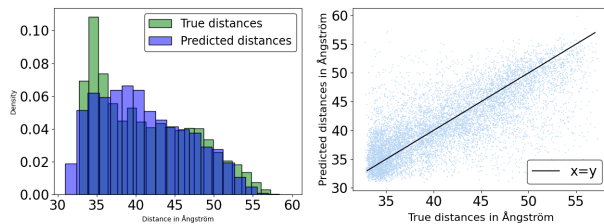
- 233
1. First, a_{ik} is successively rotated around the axis $\vec{\phi}_m$ with an angle $G_{im}\delta_m$ for $m \in \{1, \dots, N_{\text{segm}}\}$ to obtain updated coordinates a'_{ik} .
 2. Second, it is translated according to: $a''_{ik} = a'_{ik} + \sum_{j=m}^N G_{im}\vec{t}_m$.

234 This way, the transformation for a residue incorporate contributions from all segments, proportionally
235 on how much they belong to the segments. If condition (5) is met, a roughly rigid motion for
236 each segment can be expected.237 3.5 ENCODER AND PRIORS
238239 We follow the classical VAE framework. The distribution $q_\psi(y|I^*)$
240 is given by a normal distribution $\mathcal{N}(\mu(I^*), \text{diag}(\sigma^2(I^*)))$ where $\mu \in \mathbb{R}^L$
241 and $\sigma \in \mathbb{R}_+^L$ are generated by a neural network with parameters ψ , taking an
242 image I^* as input. Additionally, the approximate posterior distribution on the
243 parameters of the GMM is chosen to be Gaussian and independent of the input
244 image:

245
$$\begin{aligned} \mu_m &\sim \mathcal{N}(\nu_{\mu_m}, \beta_{\mu_m}^2) \\ \sigma_m &\sim \mathcal{N}(\nu_{\sigma_m}, \beta_{\sigma_m}^2) \\ \alpha_m &\sim \mathcal{N}(\nu_{\alpha_m}, \beta_{\alpha_m}^2) \end{aligned}$$

246 where $\{\nu_{\mu_m}, \beta_{\mu_m}, \nu_{\sigma_m}, \beta_{\sigma_m}, \nu_{\alpha_m}, \beta_{\alpha_m}\}_{m=1}^{N_{\text{segm}}}$ are parameters that are directly optimized. In practice
247 we use ELU+1 layers for σ_m to avoid negative or null standard deviation.248 Finally, we assign standard Gaussian priors to both the local latent variable $z_i \sim \mathcal{N}(0, I_L)$, and the
249 global GMM parameters $\{\mu_m, \sigma_m, \alpha_m\}_{m=1}^{N_{\text{segm}}}$. This reparameterization (Kingma & Welling, 2014)
250 is straightforward for a Gaussian distribution. Calculating the KL-divergence between two Gaussian
251 distributions as in equation 4, is also straightforward.252 3.6 LOSS
253254 Since the images may be preprocessed in unknown ways before running cryoSPHERE, we use a
255 correlation loss between predicted and ground truth image instead of a mean squared error loss,256 The decoder describes the distribution of the images given
257 the latent variables, which include:

- 258
1. One latent variable $z_i \in \mathbb{R}^L$ per image, parameterizing the conformation.
 2. The global parameters $\{\mu_m, \sigma_m, \alpha_m\}_{m=1}^{N_{\text{segm}}}$ of the GMM describing the segment decomposition.

259 Given these latent variables and a base structure S_0 , we
260 parameterize the decoder f_θ in three steps. First, a neural
261 network with parameters θ maps $z_i \in \mathbb{R}^L$ to a set of rigid262 body transformations, one for each segment $m = 1, \dots, N_{\text{segm}}$. The transformation of segment m
263 is represented by a translation vector \vec{t}_m and a unit quaternion \vec{q}_m (Vicci, 2001), which can further
264 be decomposed into an axis of rotation $\vec{\phi}_m$ and rotation angle δ_m . Second, given the parameters of
265 the GMM, we compute the matrix G . Finally, for each residue i of S_0 , we update the coordinates of
266 all its atoms $\{a_{ik}\}_{k=1}^{A_i}$:267 Figure 3: MD dataset SNR 0.001. Left: Histograms of
268 the distances of the two upper domains. The true distances
269 are in green. The recovered distances are in blue.
270 Right: Predicted against true distances in Ångström. The
271 black line represent $x = y$. The correlation between the
272 predicted and true distances is 0.73. For the same plot for
273 cryoStar, see Appendix B.2 of the supplementary file.

similar to (Li et al., 2023):

$$\mathcal{L}_{\text{corr}} = \frac{-I_i^* \cdot I(R_i, t_i, f_\theta(S_0, z))}{||I_i^*|| \times ||I(R_i, t_i, f_\theta(S_0, z))||} \quad (7)$$

where \cdot denotes the dot product. The total loss to minimize writes:

$$\mathcal{L}(I, I^*) = \mathcal{L}_{\text{corr}} + D_{\text{KL}}(q_\psi(z|I^*)||p(z)) \quad (8)$$

In our experience, it is unnecessary to add any regularization term to the correlation and KL divergence losses, except for datasets featuring a very high degree of heterogeneity. In that case, we offer the option of adding a continuity loss to avoid breaking the protein and a clashing loss to avoid clashing residues, as it is done in (Rosenbaum et al., 2021; Li et al., 2023; Jumper et al., 2021). We describe these losses in Appendix A.1 of the supplementary file.

4 RELATED WORKS

Two of the most popular methods for cryo-EM reconstruction, which are *not* based on deep learning, are RELION (Scheres, 2012) and cryoSPARC (Punjani et al., 2017). Both methods perform volume reconstruction, hypothesize that k conformations are present in the dataset and perform maximum a posteriori estimation over the k density maps, thus performing discrete heterogeneous reconstruction. Both of these algorithms operate in Fourier space using an expectation-maximization algorithm Dempster et al. (1977) and are non-amortized: the poses are refined for each image. Other approaches perform continuous heterogeneous reconstruction. For example, 3DVA (Punjani & Fleet, 2021b) uses a probabilistic principal component analysis model to learn a latent space.

Another class of methods involve deep learning and typically performs continuous heterogeneous reconstruction using a VAE architecture. Of those that attempt to reconstruct a density map, cryo-DRGN (Zhong et al., 2020; 2021a) and CryoAI (Levy et al., 2022) use a VAE acting on Fourier space to learn a latent space and a mapping that associates a 3D density map with each latent variable. They perform non-amortized and amortized inference over the poses, respectively. Other methods are defined in the image space, e.g. 3DFlex (Punjani & Fleet, 2021a) and cryoPoseNet (Nashed et al., 2021). They both perform non-amortized inference over the poses. These methods either learn, for a given image I_i , $\{V_i(x_k)\}$ the values at a set of N_{pix}^3 fixed 3D coordinates $\{x_k\}$, representing the volume on a grid (*explicit* parameterization), or they learn an actual function $\hat{V}_i : \mathbb{R}^3 \rightarrow \mathbb{R}$ in the form of a neural network that can be queried at chosen coordinates (*implicit* parameterization). These volume-based methods cannot use external structural restraints or force fields as additional information. This limits their applicability to low SNR data sets, which are frequent in protein cryo EM.

Other deep learning methods attempt to directly reconstruct structures instead of volumes and share a common process: starting from a plausible base structure, obtained with e.g. AlphaFold (Jumper et al., 2021), for each image, they move each residue of the base structure to fit the conformation present in that specific image. These methods differ on how they parameterize the structure and in the prior they impose on the deformed structure or the motion of the residues. For example AtomVAE (Rosenbaum et al., 2021) considers only residues and penalizes the distances between two subsequent residues that deviate too much from an expected value. CryoFold (Zhong et al., 2021b) considers the residue centers and their side-chain and also imposes a loss on the distances between subsequent residues and the distances between the residue centers and their side-chain. Unfortunately, due to the high level of noise and the fact that we observe only projections of the structures, these “per-residue transformation” methods tend to be stuck in local minima, yielding unrealistic conformations unless the base structure is taken from the distribution of conformations present in the images (Zhong et al., 2021b), limiting their applicability on real datasets. Even though AtomVAE (Rosenbaum et al., 2021) could roughly approximate the distribution of states of the protein, it was not able to recover the conformation given a specific image.

To reduce the bias that the base structure brings, DynaMight (Schwab et al., 2023) fits pseudo-atoms in a consensus map with a neural network directly. Similar to our work, several other methods constrain the atomic model to rigid body motions. For example e2gmm (Chen & Ludtke, 2021; Chen et al., 2023) deform a nominal structure S_0 based on how much its residues are close to a

learnt representation S_{small} of S_0 . This is similar to our GMM, except that their takes place in \mathbb{R}^3 and is not used to perform rigid body motion. Instead, they ask the user to define the segmentation in a later step. This is in contrast to cryoSPHERE, which learns the motion and the segmentation concurrently. Using DynaMight (Schwab et al., 2024), Chen et al. (2024) developed a focused refinement on patches of the GMM representation of the protein. These patches are learnt using k -means on the location of residues and do not depend on the different conformations of the data set. This in contrast to cryoSPHERE where the learning of the segments of the protein is tightly linked to the change of conformation. Concurrently to our work, Li et al. (2023) developed cryoStar which learns to translate each residue independently using a variational auto-encoder. They enforce the local rigidity of the motion of the protein by imposing a similarity loss between the base structure and the deformed structure as well as a clash loss. The interested reader can see Donnat et al. (2022) for an in-depth review of deep learning methods for cryo-EM reconstruction.

The reconstruction methods relying on an atomic model, such as cryoStar, DynaMight or cryoSPHERE offer the possibility to the user to provide prior information via this atomic model. They also offer the possibility of deforming the protein according to chemical force fields. This is not the case of the methods performing volume reconstruction without such an atomic model.

5 EXPERIMENTS

In this section, we test cryoSPHERE on a set of synthetic² and real datasets with varying level of noise and compare the results to cryoDRGN (Zhong et al., 2020) and cryoStar (Li et al., 2023). CryoDRGN is a state-of-the-art method for continuous heterogeneous reconstruction, in which the refinement occurs at the level of electron densities, while cryoStar is a structural method similar to ours. To our knowledge, the code for AtomVAE and CryoFold is not available and non-trivial to reimplement. For this reason we focus our comparison on the aforementioned methods, which have furthermore reported state-of-the-art performance. In Appendix B.1, we demonstrate that cryoSPHERE is able to recover the exact ground truth when it exists. We also discuss its performances with varying SNR and N_{segm} and show how to debias cryoSPHERE results using DRGN-AI or cryoStar volume method in Appendix B.2. Finally, Appendix B.5 compares the computational costs of cryoSPHERE and cryoStar.

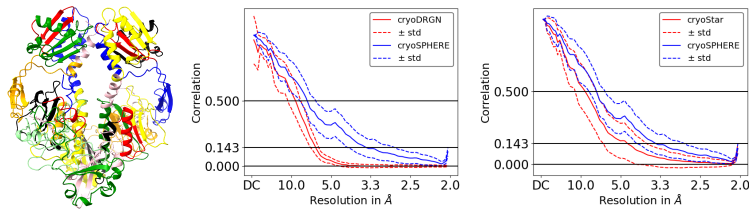


Figure 4: MD dataset. Left: cryoSPHERE Recovered segments. The colors denotes different contiguous domains. Middle and right: mean FSC comparison \pm one standard deviation, for cryoSphere and cryoDRGN and cryoStar. For a comparison between cryoStar and cryo-DRGN, see Appendix B.2 in the supplementary file.

while cryoStar is a structural method similar to ours. To our knowledge, the code for AtomVAE and CryoFold is not available and non-trivial to reimplement. For this reason we focus our comparison on the aforementioned methods, which have furthermore reported state-of-the-art performance. In Appendix B.1, we demonstrate that cryoSPHERE is able to recover the exact ground truth when it exists. We also discuss its performances with varying SNR and N_{segm} and show how to debias cryoSPHERE results using DRGN-AI or cryoStar volume method in Appendix B.2. Finally, Appendix B.5 compares the computational costs of cryoSPHERE and cryoStar.

5.1 MOLECULAR DYNAMICS DATASET: BACTERIAL PHYTOCHROME.

As a more difficult test case we simulate a continuous motion of a bacterial phytochrome, with PDB entry 4Q0J (Burgie et al., 2014). The trajectory starts at the closed conformation of Figure 11 and ends at the most open conformation on the same figure. It corresponds to a dissociation of the two top parts of the protein. This dataset has a very low SNR of 0.001. Our base structure is obtained by AlphaFold and is subsequently fitted into a homogeneous reconstruction given by the backprojection algorithm. We train cryoSPHERE with $N_{\text{segm}} = 25$, cryoStar, and cryoDRGN for 24 hours each, using the same single GPU. We get one predicted structure per image for cryoSPHERE and cryoStar, that we turn into volumes using (1), and one predicted volume per image for cryoDRGN. See Appendix B.2 in the supplementary file for details and comparison with different values of N_{segm} . Note that since both cryoSPHERE and cryoStar use a nominal structure, we fit the structure we obtained through AlphaFold in the consensus reconstruction obtained by backprojection and use that exact same structure as the nominal one for both methods.

²See Appendix B of the supplementary file for details on how we created the synthetic datasets.

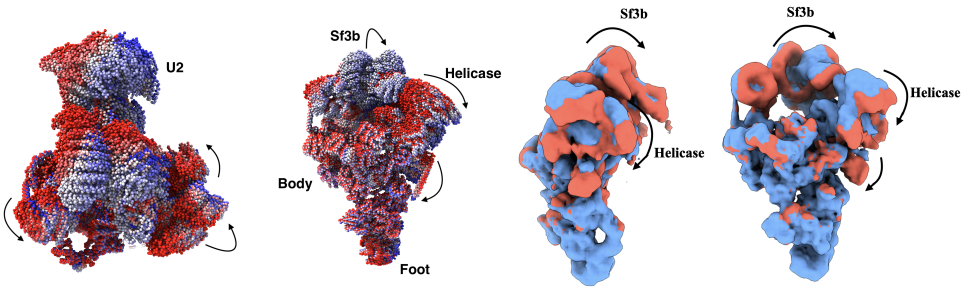


Figure 5: EMPIAR10180. Left and middle left: different views of the structures corresponding to the red dots of Figure 48. The motion goes from red (left in the first principal component) to white to blue (right of the principal component). Only the C_α atoms are shown. Right and middle right: different views of two volumes recovered by training DRGN-AI on the latent space of cryoSPHERE. The U2 domain disappears on the volume because of a compositional heterogeneity.

Figure 3 shows the predicted distance between the two upper parts of the protein being dissociated, against the ground truth distance for each image. In spite of the very low SNR, cryoSPHERE roughly recovers the right distribution of distances. More importantly, the correlation between the predicted distance and ground truth distance is 0.74, showing that cryoSPHERE is able to recover the correct conformation given an image. This is in stark contrast with Rosenbaum et al. (2021) who could not recover the conformation conditionally on an image. In addition, our model has learnt to separate the two mobile top domains from the fix bottom one, as shown by the segment decomposition in Figure 4. Appendix B.2 in the supplementary file shows the same figures for cryoStar.

We plot the mean of the FSC curves between the predicted volumes and the corresponding ground truth volumes in Figure 4, for cryoSPHERE, cryoDRGN and cryoStar. CryoSPHERE performs better than both cryoDRGN and cryoStar at both the 0.5 and 0.143 cutoffs. We attribute this to three key properties. Firstly, we fit our base structure into a consensus reconstruction. This step corrects the position of the medium-scale elements of the base structure that could have been misplaced, boosting the FSC of cryoSPHERE at the 0.5 cutoff. Secondly, acting directly on the structure level offers a finer resolution than cryoDRGN given the level of noise. Figure 32 shows that cryoDRGN underestimated the opening of the protein and sometimes gives very noisy volumes. That explain why we outperform cryoDRGN at the 0.143 cutoff. Finally, cryoSPHERE is rigidly moving larger segments of the protein. This provide a better resistance to high levels of noise and overfitting compared to moving each residue individually like cryoStar does, providing a possible explanation to the improvement compared to cryoStar at the 0.143 cutoff.

5.2 EMPIAR 10180

We now demonstrate that cryoSPHERE is applicable to real data as well as large proteins. We run cryoSPHERE on EMPIAR-10180 Plaschka et al. (2017), comprising 327 490 images of a pre-catalytic spliceosome with 13 941 residues, making it a computationally heavy dataset to tackle. We use the atomic model by Plaschka et al. (2017) (PDB: 5NRL).

Figure 5 shows a set of ten structures taken evenly along the first principal component of the latent space. To interrogate if these structures contain bias from the structural constraints, we perform a volume reconstruction step similar to cryoStar Phase II, see Figure 5.

Traversing the first principal component shows that the Sf3b domain gets incurvated down while the helicase move closer to the foot of the protein. This is in line with the literature (Li et al., 2023; Plaschka et al., 2017). The motion of the protein also brings the alpha helix of the Spp381 domain closer to the foot, as corroborated by Li et al. (2023). Comparison between the recovered structures and volumes (Figure 50) shows similar movements, indicating a small amount of bias from the structural constraints. In addition, the absence of density corresponding to the U2 domain in the volume indicates that there is compositional heterogeneity that cryoSPHERE could not detect, see Figure 5. We provide a movie of the motion and more structures and volumes in appendix B.3 in the supplementary file.

5.3 EMPIAR-12093

We now tackle the recently published EMPIAR-12093 (Bódizs et al., 2024). This dataset comprises two sets of images: one non-activated (Pfr) and one activated (Pr). These dataset are very challeng-

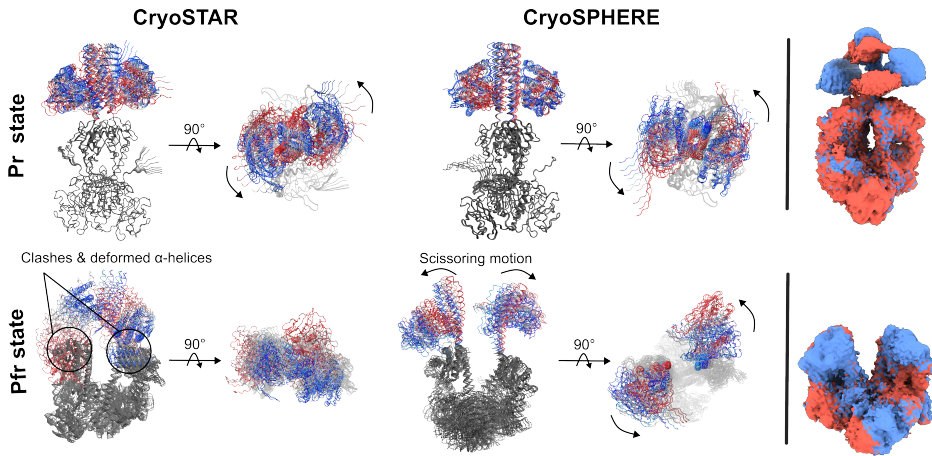


Figure 6: EMPIAR12093. Left of the black line: Ten structures sampled along PC1, for cryoSPHERE and cryoStar. Right of the black line: examples of volumes reconstructed by training the cryoStar volume method on the latent space of cryoSPHERE for debiasing. The blue and red volumes correspond to the first and last volumes along PC1. Top row corresponds to Pr; bottom row to Pfr.

ing because of the high level of noise and heterogeneity of the protein, especially in the Pfr dataset. Traditional methods like cryoSparc (Punjani et al., 2017) or cryoDRGN (Zhong et al., 2020; 2021a) fail at reconstructing the upper part of the protein, see Bódizs et al. (2024) and Appendix B.4.

Figure 6 shows principal component 1 traversal for cryoStar and cryoSPHERE. For Pr, both methods are in strong agreement and reveal a rotation of the upper domain around its axis, while the lower part remains stationary. This aligns with previous studies (Wahlgren et al.; Malla et al., 2024)).

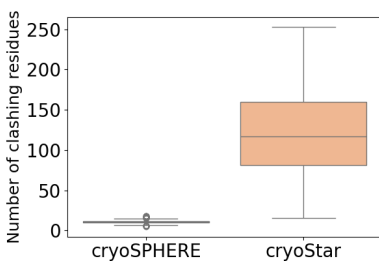


Figure 7: EMPIAR12093. Distribution of the number of clashes for 2000 randomly chosen structures Pfr dataset, for cryoSPHERE and cryoStar. Two non contiguous residues are said to be clashing if their distance is less than 4 Å.

Analysis of the dataset on phytochromes illustrates the scope and limitations of the different methods. Pure image-based methods (i.e. cryo DRGN) already fail on the Pr state with its intermediate disorder, while cryoSTAR and cryoSPHERE succeed in obtaining reasonable reconstructions (Figure 6). For the Pfr state it becomes evident that cryoSTAR struggles with the high noise and large motions encoded in the dataset. Its deformation-based approach results in unphysical motions along the first principal component, often leading to structural clashes. In contrast, cryoSPHERE handles the noise effectively, producing physically plausible large-scale motions in both the upper and lower domains, see Figure 7, the supplementary movies and B.4. We assign this superior performance to the higher degree of structural constraints that are used in cryoSPHERE compared to cryoSTAR.

We also performed debiasing of cryoSPHERE with a volume method and show examples of reconstructed volumes in Figure 6. For Pr, recovered densities are visible for the entire protein and confirm the dynamics of the upper domains, confirming the absence of compositional heterogeneity and a minimum of bias due to structural constraints. However, for Pfr, meaningful density of the upper (dynamic) part of the protein cannot be recovered, because the signal level in the averaged

486 density is too low. Thus, for this most dynamic protein case, volume-based debiasing is not possible,
 487 despite the fact that the structure based cryoSPHERE finds solutions that fit the data set.
 488

489 6 DISCUSSION 490

491 CryoSPHERE presents several advantages compared to other methods for volume and structure
 492 reconstruction.
 493

494 **Efficiency in Deformation:** Deforming a base structure into a density map avoids the computa-
 495 tionally expensive N_{pix}^2 evaluation required by a decoder neural network in methods implicitly
 496 parameterising the grid, such as Zhong et al. (2021a); Levy et al. (2022). Furthermore, direct defor-
 497 mation of a structure directly avoids the need for subsequent fitting into the recovered density map.

498 **Reduced Dimensionality and Noise Resilience:** Learning one rigid transformation per segment,
 499 where the number of segments is much smaller than the number of residues, reduces the dimen-
 500 sionality of the problem. This results in a smaller neural network size compared to approaches acting
 501 on each residues, such as Rosenbaum et al. (2021). Rigidly moving large portions of the protein
 502 corresponds to low-frequency movements, less prone to noise pollution than the high-frequency
 503 movements associated with moving each residue independently. In addition, since our goal is to
 504 learn one rotation and one translation per segment, a latent variable of dimension $6 \times N_{\text{segm}}$ is, in
 505 principle, a sufficiently flexible choice to model any transformation of the base structure. Choos-
 506 ing the latent dimension is more difficult for volume reconstruction methods such as (Zhong et al.,
 507 2021a).

508 **Interpretability:** CryoSPHERE outputs segments along with one rotation and one translation per
 509 segment, providing valuable and interpretable information. Practitioners can easily interpret how
 510 different parts are moving based on the transformations the network outputs. This interpretability is
 511 often challenging for deep learning models such as Zhong et al. (2021a); Rosenbaum et al. (2021).

512 Section 5 and Appendix B.2 demonstrate cryoSPHERE’s capability to recover conformational het-
 513 erogeneity while performing structure reconstruction. The division into N_{segm} is learned from the
 514 data and only marginally impacts the FSC to the ground truth. Moreover, cryoSPHERE recovers
 515 the correct motion for the entire range of N_{segm} values and is able to keep the minimum necessary
 516 number of domains when the user sets it too high (Appendix B.1).

517 **Structural restraints allow interpretation of low SNR datasets:** It is evident that structural re-
 518 straints as implemented in cryoSPHERE (this work) and cryoSTAR provide additional restraints that
 519 pure volume methods (i.e. cryoDRGN) lacks, thus giving better reconstructions for high noise data
 520 sets. The additional restraints may introduce bias, which needs to be alleviated using a backprojec-
 521 tion algorithm. This, combined with cryoSPHERE’s latent space, achieves better 0.5 cutoffs than
 522 cryoDRGN, indicating its effectiveness in resolving conformational heterogeneity and debiasing the
 523 results. If such a volume is unavailable, simply increasing N_{segm} can reduce the bias. As a note
 524 of caution we find that for most dynamic protein studies here (the Pfr state of the phytochrome),
 525 we find that volume-based debiasing fails because of the very low electron density levels in the
 526 reconstructions. Here, other metrics should be developed in the future.

527 **Summary:** Our study opens up for significant advancements in predicting protein ensembles and
 528 dynamics, critically important for unraveling the complexity of biological systems. By predicting
 529 all-atom structures from cryo-EM datasets through more realistic deformations, our work lays the
 530 foundation for extracting direct insights into thermodynamic and kinetic properties. This work is an
 531 important milestone in showing that one can learn a segmentation of the protein that is intimately
 532 linked to the change of conformation of the underlying protein, in an end-to-end fashion. In the
 533 future, we anticipate the ability to predict rare and high-energy intermediate states, along with their
 534 kinetics, a feat beyond the reach of conventional methods such as molecular dynamics simulations.
 535

536 It would be interesting to assess how much our segmentation correlates with bottom-up segmen-
 537 tation into domains conducted on the “omics” scale, see e.g. Lau et al. (2023). To achieve this
 538 quantitatively, we would need many examples of moving segments from cryo-EM investigations to
 539 match the millions of segments from the “omics” studies. Therefore, we leave this investigation to
 later work.

540 **7 REPRODUCIBILITY STATEMENT**
 541

542 As part of the current paper, we provide a github link to the source code in Section 1. We also
 543 describe in detail how we generate the synthetic datasets in Appendix B.2 and the hyperparameters
 544 chosen to run cryoStar, cryoSPHERE and cryoDRGN in Appendix B for each of the experiments.
 545

546 **REFERENCES**
 547

- 548 Mark James Abraham, Teemu Murtola, Roland Schulz, Szilárd Páll, Jeremy C. Smith, Berk Hess,
 549 and Erik Lindahl. GROMACS: High performance molecular simulations through multi-level
 550 parallelism from laptops to supercomputers. *SoftwareX*, 1-2:19–25, September 2015. ISSN
 551 2352-7110. doi: 10.1016/j.softx.2015.06.001. URL <https://www.sciencedirect.com/science/article/pii/S2352711015000059>.
 552
- 553 Minkyung Baek, Frank DiMaio, Ivan Anishchenko, Justas Dauparas, Sergey Ovchinnikov, Gyu Rie
 554 Lee, Jue Wang, Qian Cong, Lisa N. Kinch, R. Dustin Schaeffer, Claudia Millán, Hahnbeom
 555 Park, Carson Adams, Caleb R. Glassman, Andy DeGiovanni, Jose H. Pereira, Andria V. Ro-
 556 drigues, Alberdina A. van Dijk, Ana C. Ebrecht, Diederik J. Opperman, Theo Sagmeister,
 557 Christoph Buhlheller, Tea Pavkov-Keller, Manoj K. Rathinaswamy, Udit Dalwadi, Calvin K. Yip,
 558 John E. Burke, K. Christopher Garcia, Nick V. Grishin, Paul D. Adams, Randy J. Read, and
 559 David Baker. Accurate prediction of protein structures and interactions using a three-track neu-
 560 ral network. *Science*, 373(6557):871–876, August 2021. doi: 10.1126/science.abj8754. URL
 561 <https://www.science.org/doi/10.1126/science.abj8754>. Publisher: Ameri-
 562 can Association for the Advancement of Science.
 563
- 563 Alessandro Barducci, Massimiliano Bonomi, and Michele Parrinello. Metadynamics. *WIREs Com-
 564 putational Molecular Science*, 1(5):826–843, 2011. ISSN 1759-0884. doi: 10.1002/wcms.31.
 565 URL <https://onlinelibrary.wiley.com/doi/abs/10.1002/wcms.31>. eprint:
 566 <https://onlinelibrary.wiley.com/doi/pdf/10.1002/wcms.31>.
 567
- 567 E. Sethe Burgie, Tong Wang, Adam N. Bussell, Joseph M. Walker, Huilin Li, and Richard D. Vier-
 568 stra. Crystallographic and electron microscopic analyses of a bacterial phytochrome reveal local
 569 and global rearrangements during photoconversion. *The Journal of Biological Chemistry*, 289
 570 (35):24573–24587, August 2014. ISSN 1083-351X. doi: 10.1074/jbc.M114.571661.
 571
- 571 Szabolcs Bódizs, Petra Mészáros, Lukas Grunewald, Heikki Takala, and Sebastian Westenhoff.
 572 Cryo-EM structures of a bathy phytochrome histidine kinase reveal a unique light-dependent ac-
 573 tivation mechanism. *Structure (London, England: 1993)*, 32(11):1952–1962.e3, November 2024.
 574 ISSN 1878-4186. doi: 10.1016/j.str.2024.08.008.
 575
- 576 Muyuan Chen and Steven J. Ludtke. Deep learning-based mixed-dimensional Gaussian mixture
 577 model for characterizing variability in cryo-EM. *Nature Methods*, 18(8):930–936, August 2021.
 578 ISSN 1548-7105. doi: 10.1038/s41592-021-01220-5. URL <https://www.nature.com/articles/s41592-021-01220-5>. Number: 8 Publisher: Nature Publishing Group.
 579
- 580 Muyuan Chen, Bogdan Toader, and Roy Lederman. Integrating Molecular Models Into Cry-
 581 oEM Heterogeneity Analysis Using Scalable High-resolution Deep Gaussian Mixture Mod-
 582 els. *Journal of Molecular Biology*, 435(9):168014, May 2023. ISSN 00222836. doi:
 583 10.1016/j.jmb.2023.168014. URL <https://linkinghub.elsevier.com/retrieve/pii/S0022283623000700>.
 584
- 585 Muyuan Chen, Michael F. Schmid, and Wah Chiu. Improving resolution and resolvability of
 586 single-particle cryoEM structures using Gaussian mixture models. *Nature Methods*, 21(1):37–
 587 40, January 2024. ISSN 1548-7091, 1548-7105. doi: 10.1038/s41592-023-02082-9. URL
 588 <https://www.nature.com/articles/s41592-023-02082-9>.
 589
- 590 A. P. Dempster, N. M. Laird, and D. B. Rubin. Maximum Likelihood from Incomplete Data
 591 Via the EM Algorithm. *Journal of the Royal Statistical Society: Series B (Methodologi-
 592 cal)*, 39(1):1–22, 1977. ISSN 2517-6161. doi: 10.1111/j.2517-6161.1977.tb01600.x. URL
 593 <https://onlinelibrary.wiley.com/doi/abs/10.1111/j.2517-6161.1977.tb01600.x>. eprint:
 <https://onlinelibrary.wiley.com/doi/pdf/10.1111/j.2517-6161.1977.tb01600.x>.

- 594 Claire Donnat, Axel Levy, Frédéric Poitevin, Ellen D. Zhong, and Nina Miolane. Deep generative modeling for volume reconstruction in cryo-electron microscopy. *Journal of Structural Biology*, 214(4):107920, December 2022. ISSN 1047-8477. doi: 10.1016/j.jsb.2022.107920. URL <https://www.sciencedirect.com/science/article/pii/S1047847722000909>.
- 595
- 596
- 597
- 598
- 599 Richard Evans, Michael O'Neill, Alexander Pritzel, Natasha Antropova, Andrew Senior, Tim Green, Augustin Žídek, Russ Bates, Sam Blackwell, Jason Yim, Olaf Ronneberger, Sebastian Bodenstein, Michal Zielinski, Alex Bridgland, Anna Potapenko, Andrew Cowie, Kathryn Tunyasuvunakool, Rishabh Jain, Ellen Clancy, Pushmeet Kohli, John Jumper, and Demis Hassabis. Protein complex prediction with AlphaFold-Multimer. preprint, Bioinformatics, October 2021. URL <http://biorxiv.org/lookup/doi/10.1101/2021.10.04.463034>.
- 600
- 601
- 602
- 603
- 604
- 605
- 606 John Jumper, Richard Evans, Alexander Pritzel, Tim Green, Michael Figurnov, Olaf Ronneberger, Kathryn Tunyasuvunakool, Russ Bates, Augustin Žídek, Anna Potapenko, Alex Bridgland, Clemens Meyer, Simon A. A. Kohl, Andrew J. Ballard, Andrew Cowie, Bernardino Romera-Paredes, Stanislav Nikolov, Rishabh Jain, Jonas Adler, Trevor Back, Stig Petersen, David Reiman, Ellen Clancy, Michal Zielinski, Martin Steinegger, Michalina Pacholska, Tamas Berghammer, Sebastian Bodenstein, David Silver, Oriol Vinyals, Andrew W. Senior, Koray Kavukcuoglu, Pushmeet Kohli, and Demis Hassabis. Highly accurate protein structure prediction with AlphaFold. *Nature*, 596(7873):583–589, August 2021. ISSN 1476-4687. doi: 10.1038/s41586-021-03819-2. URL <https://www.nature.com/articles/s41586-021-03819-2>.
- 614
- 615 Diederik P. Kingma and Jimmy Ba. Adam: A Method for Stochastic Optimization, January 2017.
- 616 URL <http://arxiv.org/abs/1412.6980>. arXiv:1412.6980 [cs].
- 617
- 618 Diederik P. Kingma and Max Welling. Auto-Encoding Variational Bayes, May 2014. URL <http://arxiv.org/abs/1312.6114>.
- 619
- 620
- 621 Andy M. Lau, Shaun M. Kandathil, and David T. Jones. Merizo: a rapid and accurate protein domain segmentation method using invariant point attention. *Nature Communications*, 14(1):8445, December 2023. ISSN 2041-1723. doi: 10.1038/s41467-023-43934-4. URL <https://www.nature.com/articles/s41467-023-43934-4>.
- 622
- 623
- 624
- 625 Axel Levy, Frédéric Poitevin, Julien Martel, Youssef Nashed, Ariana Peck, Nina Miolane, Daniel Ratner, Mike Dunne, and Gordon Wetzstein. CryoAI: Amortized Inference of Poses for Ab Initio Reconstruction of 3D Molecular Volumes from Real Cryo-EM Images. In Shai Avidan, Gabriel Brostow, Moustapha Cissé, Giovanni Maria Farinella, and Tal Hassner (eds.), *Computer Vision – ECCV 2022*, Lecture Notes in Computer Science, pp. 540–557, Cham, 2022. Springer Nature Switzerland. ISBN 978-3-031-19803-8. doi: 10.1007/978-3-031-19803-8_32.
- 626
- 627
- 628
- 629
- 630
- 631 Axel Levy, Michal Grzadkowski, Frédéric Poitevin, Francesca Vallese, Oliver Biggs Clarke, Gordon Wetzstein, and Ellen D. Zhong. Revealing biomolecular structure and motion with neural ab initio cryo-em reconstruction. *bioRxiv*, 2024. doi: 10.1101/2024.05.30.596729. URL <https://www.biorxiv.org/content/early/2024/06/02/2024.05.30.596729>.
- 632
- 633
- 634
- 635
- 636 Yilai Li, Yi Zhou, Jing Yuan, Fei Ye, and Quanquan Gu. CryoSTAR: Leveraging Structural Prior and Constraints for Cryo-EM Heterogeneous Reconstruction, November 2023. URL <https://www.biorxiv.org/content/10.1101/2023.10.31.564872v1>. Pages: 2023.10.31.564872 Section: New Results.
- 637
- 638
- 639
- 640 Tek Narsingh Malla, Carolina Hernandez, Srinivasan Muniyappan, David Menendez, Dorina Bizega, Joshua H. Mendez, Peter Schwander, Emina A. Stojković, and Marius Schmidt. Photoreception and signaling in bacterial phytochrome revealed by single-particle cryo-em. *Science Advances*, 10(32):eadq0653, 2024. doi: 10.1126/sciadv.adq0653. URL <https://www.science.org/doi/abs/10.1126/sciadv.adq0653>.
- 641
- 642
- 643
- 644
- 645
- 646 Andreas Mardt, Tim Hempel, Cecilia Clementi, and Frank Noé. Deep learning to decompose macromolecules into independent Markovian domains. preprint, Biophysics, March 2022. URL <http://biorxiv.org/lookup/doi/10.1101/2022.03.30.486366>.
- 647

- 648 Shakir Mohamed, Mihaela Rosca, Michael Figurnov, and Andriy Mnih. Monte Carlo Gradient
 649 Estimation in Machine Learning. 2019. doi: 10.48550/ARXIV.1906.10652. URL <https://arxiv.org/abs/1906.10652>. Publisher: [object Object] Version Number: 2.
 650
- 651 Youssef S. G. Nashed, Frédéric Poitevin, Harshit Gupta, Geoffrey Woppard, Michael Kagan,
 652 Chun Hong Yoon, and Daniel Ratner. CryoPoseNet: End-to-End Simultaneous Learning of
 653 Single-particle Orientation and 3D Map Reconstruction from Cryo-electron Microscopy Data. In
 654 *2021 IEEE/CVF International Conference on Computer Vision Workshops (ICCVW)*, pp. 4049–
 655 4059, October 2021. doi: 10.1109/ICCVW54120.2021.00452. URL <https://ieeexplore.ieee.org/document/9607470>. ISSN: 2473-9944.
 656
- 657 David L. Nelson, Michael M. Cox, and Albert L. Lehninger. *Lehninger principles of biochemistry*.
 658 Macmillan learning. W.H. Freeman, New York NY, seventh edition edition, 2017. ISBN 978-1-
 659 319-10824-3 978-1-4641-2611-6.
 660
- 661 Clemens Plaschka, Pei-Chun Lin, and Kiyoshi Nagai. Structure of a pre-catalytic spliceosome.
 662 *Nature*, 546(7660):617–621, June 2017. ISSN 1476-4687. doi: 10.1038/nature22799. URL
 663 <https://doi.org/10.1038/nature22799>.
 664
- 665 Sander Pronk, Szilárd Páll, Roland Schulz, Per Larsson, Pär Bjelkmar, Rossen Apostolov,
 666 Michael R. Shirts, Jeremy C. Smith, Peter M. Kasson, David van der Spoel, Berk Hess, and
 667 Erik Lindahl. GROMACS 4.5: a high-throughput and highly parallel open source molecular sim-
 668 ulation toolkit. *Bioinformatics (Oxford, England)*, 29(7):845–854, April 2013. ISSN 1367-4811.
 669 doi: 10.1093/bioinformatics/btt055.
 670
- 671 Ali Punjani and David J. Fleet. 3D Flexible Refinement: Structure and Motion of Flexible Proteins
 672 from Cryo-EM, April 2021a. URL <https://www.biorxiv.org/content/10.1101/2021.04.22.440893v1>.
 673
- 674 Ali Punjani and David J. Fleet. 3D variability analysis: Resolving continuous flexibility and
 675 discrete heterogeneity from single particle cryo-EM. *Journal of Structural Biology*, 213(2):
 676 107702, June 2021b. ISSN 1047-8477. doi: 10.1016/j.jsb.2021.107702. URL <https://www.sciencedirect.com/science/article/pii/S1047847721000071>.
 677
- 678 Ali Punjani, John L. Rubinstein, David J. Fleet, and Marcus A. Brubaker. cryoSPARC: algorithms
 679 for rapid unsupervised cryo-EM structure determination. *Nature Methods*, 14(3):290–296, March
 680 2017. ISSN 1548-7105. doi: 10.1038/nmeth.4169. URL <https://www.nature.com/articles/nmeth.4169>. Number: 3 Publisher: Nature Publishing Group.
 681
- 682 Dan Rosenbaum, M. Garnelo, Michal Zielinski, Charlie Beattie, Ellen Clancy, Andrea Hu-
 683 ber, Pushmeet Kohli, A. Senior, J. Jumper, Carl Doersch, S. Eslami, O. Ronneberger, and
 684 J. Adler. Inferring a Continuous Distribution of Atom Coordinates from Cryo-EM Images
 685 using VAEs. *ArXiv*, June 2021. URL <https://www.semanticscholar.org/paper/Inferring-a-Continuous-Distribution-of-Atom-from-Rosenbaum-Garnelo/68c5ef8006fe531fba4362d601364ea00791da51>.
 686
- 687 Sjors H. W. Scheres. RELION: Implementation of a Bayesian approach to cryo-EM structure de-
 688 termination. *Journal of Structural Biology*, 180(3):519–530, December 2012. ISSN 1047-8477.
 689 doi: 10.1016/j.jsb.2012.09.006. URL <https://www.sciencedirect.com/science/article/pii/S1047847712002481>.
 690
- 691 Georg E. Schulz and R. Heiner Schirmer. *Principles of Protein Structure*. Springer Advanced
 692 Texts in Chemistry. Springer New York, New York, NY, 1979. ISBN 978-0-387-90334-7 978-1-
 693 4612-6137-7. doi: 10.1007/978-1-4612-6137-7. URL <http://link.springer.com/10.1007/978-1-4612-6137-7>.
 694
- 695 Johannes Schwab, Dari Kimanis, Alister Burt, Tom Dendooven, and Sjors H.W. Scheres. Dy-
 696 naMight: estimating molecular motions with improved reconstruction from cryo-EM images,
 697 October 2023. URL <http://biorxiv.org/lookup/doi/10.1101/2023.10.18.562877>.
 698

- 702 Johannes Schwab, Dari Kimanis, Alister Burt, Tom Dendooven, and Sjors H. W. Scheres. Dy-
 703 naMight: estimating molecular motions with improved reconstruction from cryo-EM images.
 704 *Nature Methods*, pp. 1–8, August 2024. ISSN 1548-7105. doi: 10.1038/s41592-024-02377-5.
 705 URL <https://www.nature.com/articles/s41592-024-02377-5>. Publisher: Na-
 706 ture Publishing Group.
- 707 Heikki Takala, Alexander Björling, Oskar Berntsson, Heli Lehtivuori, Stephan Niebling, Maria
 708 Hoernke, Irina Kosheleva, Robert Henning, Andreas Menzel, Janne A. Ihalainen, and Sebas-
 709 tian Westenhoff. Signal amplification and transduction in phytochrome photosensors. *Na-*
 710 *nature*, 509(7499):245–248, May 2014. ISSN 1476-4687. doi: 10.1038/nature13310. URL
 711 <https://www.nature.com/articles/nature13310>. Publisher: Nature Publishing
 712 Group.
- 713 The UniProt Consortium. UniProt: the universal protein knowledgebase in 2021. *Nucleic Acids
 714 Research*, 49(D1):D480–D489, January 2021. ISSN 0305-1048. doi: 10.1093/nar/gkaa1100.
 715 URL <https://doi.org/10.1093/nar/gkaa1100>.
- 716 Gareth A. Tribello, Massimiliano Bonomi, Davide Branduardi, Carlo Camilloni, and Giovanni
 717 Bussi. PLUMED 2: New feathers for an old bird. *Computer Physics Communications*, 185
 718 (2):604–613, February 2014. ISSN 0010-4655. doi: 10.1016/j.cpc.2013.09.018. URL <https://www.sciencedirect.com/science/article/pii/S0010465513003196>.
- 719 Leandra Vicci. Quaternions and Rotations in 3-Space: The Algebra and its Geometric Interpretation.
 720 June 2001.
- 721 Miloš Vulović, Raimond B. G. Ravelli, Lucas J. van Vliet, Abraham J. Koster, Ivan Lazić, Uwe
 722 Lücke, Hans Rullgård, Ozan Öktem, and Bernd Rieger. Image formation modeling in cryo-
 723 electron microscopy. *Journal of Structural Biology*, 183(1):19–32, July 2013. ISSN 1095-8657.
 724 doi: 10.1016/j.jsb.2013.05.008.
- 725 Weixiao Yuan Wahlgren, Elin Claesson, Iida Kettunen, Sergio Trillo-Muyo, Szabolcs Bodizs,
 726 Janne A. Ihalainen, Heikki Takala, and Westenhoff Sebastian. Structural mechanism of signal
 727 transduction kinase.
- 728 Ellen D. Zhong, Tristan Bepler, Joseph H. Davis, and Bonnie Berger. Reconstructing continuous
 729 distributions of 3D protein structure from cryo-EM images, February 2020. URL <http://arxiv.org/abs/1909.05215>.
- 730 Ellen D. Zhong, Adam Lerer, Joseph H. Davis, and Bonnie Berger. CryoDRGN2: Ab initio
 731 neural reconstruction of 3D protein structures from real cryo-EM images. In 2021 IEEE/CVF
 732 International Conference on Computer Vision (ICCV), pp. 4046–4055, October 2021a. doi:
 733 10.1109/ICCV48922.2021.00403. URL <https://ieeexplore.ieee.org/document/9710804>. ISSN: 2380-7504.
- 734 Ellen D. Zhong, Adam Lerer, Joseph H. Davis, and Bonnie Berger. Exploring generative atomic
 735 models in cryo-EM reconstruction, July 2021b. URL <http://arxiv.org/abs/2107.01331>. arXiv:2107.01331 [q-bio].
- 736
 737
 738
 739
 740
 741
 742
 743
 744
 745
 746
 747
 748
 749
 750
 751
 752
 753
 754
 755